

ARTICLE

Open Access

# Achieving structural white inspired by quasiordered microstructures in *Morpho theseus*

Xinkun Zhao<sup>1</sup>, Yuqin Xiong<sup>1</sup>, Wanlin Wang<sup>2</sup>, Wang Zhang<sup>1</sup> and Di Zhang<sup>1</sup>

## Abstract

As one of the most fascinating phenomena, structural whiteness in natural organisms serves important functions in thermoregulation and mating. However, the architectures that cause visible broadband reflection are often in quasiordered distributions, which hinders systematic research on their color formation mechanisms. Here, through numerical analysis, the architectures in *Morpho theseus* scales are shown to be distributed in various tubular morphologies between tubular and gyroid structures. Then, the mechanism of structural white is discussed using the numerical model built with the combination of a periodic numerical framework and random elements. Thermodynamic experiments indicate that the white scales can efficiently help reduce the temperature of butterfly wings under a direct light beam. Our work provides a concise method for analyzing quasiordered structures. The methodology developed by this numerical model can facilitate a deep understanding of the performance improvement facilitated by these structural characteristics. Corresponding solutions can guide the design of nano-optical materials to achieve an efficient cooling, camouflage, and photothermal conversion system.

## Introduction

Through a billion years of accretion, nature has provided abundant inspiration for the design of materials with specific microstructures<sup>1–4</sup>. As one of the many fascinating natural phenomena, structural whiteness exists in many organisms, which provides valuable ideas for industrial products and cooling solutions<sup>5–8</sup>. Compared with white pigments and high-refractive-index particles (e.g., ZnO, ZrO<sub>2</sub>, TiO<sub>2</sub>), structurally white architectures are environmentally friendly and diminish the intrinsic optical properties of materials with even thinner layers<sup>9</sup>. According to light scattering intensity and angle dependence, structural whiteness can be divided into two categories: (1) uniform white, of which the reflection intensity is relatively low and angle independent. The relevant structures tend to be disordered, such as micropores<sup>10,11</sup>, nanoparticles<sup>12,13</sup>,

disorganized networks<sup>14,15</sup>, and structural combinations<sup>16,17</sup>; and (2) metallic white, which is widely found in insects, such as butterflies and beetles. The shining effect caused by periodic architectures is useful for attracting mates<sup>18,19</sup>. In addition, in a handful of species living in high-temperature areas, the presence of scales or hairs on the body surface effectively dissipates heat<sup>5,20</sup>. These findings also provide inspiration for low-cost cooling applications.

In consideration of the potential of structural whiteness, comprehensive numerical studies have been performed to understand the relevant optical mechanisms<sup>21–23</sup>. The recent proposal of the unified evolving model based on trigonometric implicit functions has revealed the connection between different structures and greatly improved the simulation efficiency<sup>24</sup>. For disordered structures, it is challenging to simulate optical mechanisms, although it is crucial for cooling device design. In particular, the microstructures in nature are often distributed in quasiordered form. There is a lack of a numerical model that addresses this kind of characteristic.

Lepidopteran scales exhibit exquisite architectures for multiple survival strategies, such as heat management,

Correspondence: Wanlin Wang ([wangwanlin@szu.edu.cn](mailto:wangwanlin@szu.edu.cn)) or Wang Zhang ([wangzhang@sjtu.edu.cn](mailto:wangzhang@sjtu.edu.cn))

<sup>1</sup>State Key Laboratory of Metal Matrix Composite, Shanghai Jiao Tong University, 200240 Shanghai, China

<sup>2</sup>College of Electronics and Information Engineering, Shenzhen University, 518060 Shenzhen, Guangdong, China

© The Author(s) 2023



**Open Access** This article is licensed under a Creative Commons Attribution 4.0 International License, which permits use, sharing, adaptation, distribution and reproduction in any medium or format, as long as you give appropriate credit to the original author(s) and the source, provide a link to the Creative Commons license, and indicate if changes were made. The images or other third party material in this article are included in the article's Creative Commons license, unless indicated otherwise in a credit line to the material. If material is not included in the article's Creative Commons license and your intended use is not permitted by statutory regulation or exceeds the permitted use, you will need to obtain permission directly from the copyright holder. To view a copy of this license, visit <http://creativecommons.org/licenses/by/4.0/>.

courtship, and camouflage<sup>25–28</sup>. *Morpho theseus juturna*, a Neotropical butterfly mainly living in Central America, is particularly noticeable owing to the dense bright white scales covering almost all the ventral region. With long-term exposure to a hot environment<sup>29</sup>, the white patch on the body of this butterfly can reflect most sunlight to avoid overheating in the daytime.

In this study, we discovered that the bright white color of *M. theseus* is caused by quasicrystalline tubular structures in its scales, which exist in different orientations and twinning forms. This is similar to the state before the early morphology of the gyroid structure in *Callophrys rubi*. The tubular characteristics are in accordance with the spatial structure represented by the trigonometric function  $\sin(x)\cos(y) = t$ , which precisely matches the fundamental numerical element in the gyroid model<sup>30</sup>. Then, a numerical model was built to characterize the quasicrystalline architectures in *M. theseus* wing scales. The simulated optical results based on the finite-difference time-domain (FDTD) method indicated that the different morphologies between the tubular and gyroid structures caused a color mixing effect. This effect appears as a broadband reflection in the visible light spectrum from the macroscopic view. Furthermore, we found that the microstructures in the scales effectively reduced body temperature through surface thermal measurements, which raises the survival rate of *M. theseus* in tropical regions. Our work reveals the mathematical correlation between high-ordered and quasicrystalline structures. The numerical model can facilitate a deep understanding of the performance improvement facilitated by a quasicrystalline microstructure. Corresponding solutions will guide the refinement of vital biological structures combined with optimized artificial materials to be applied in the fields of photonic devices.

## Methods

### Specimen characterizations

Specimens of *M. theseus* and *C. rubi* were acquired from Shanghai Dieyu Corporation, China. Optical images of the original butterfly scales were taken by an extended depth-of-field optical microscope (KEYENCE VHX-1000E) with the light source of a halogen lamp (12 V, 100 W). The reflectance spectra of the original *M. theseus* and *C. rubi* wing scales were measured with a microspectrograph (NOVA, IdeoOptics). The microangular dependency of *M. theseus* scales was determined with a microscopic angle-resolved spectral system (ARM, angle-resolved spectrum system in microregion, IdeoOptics) with a spot diameter of 30  $\mu\text{m}$ . The angle detection range was from  $-60^\circ$  to  $+60^\circ$  with a step of  $1^\circ$ . Sections of  $6 \times 6$  mm were cut from *M. theseus* and *C. rubi* wings and placed on aluminum stubs using copper tape, sputter-coated with gold for 15 s (Q150T ES plus), and then observed with scanning electron

microscopy (SEM, TESCAN-MIRA3). Images of the scale cross-sections were acquired using transmission electron microscopy (TEM, Bio-TEM FEI Tecnai G2 Spirit Biotwin).

### TEM projections

The TEM cross-section samples (*M. theseus* and *C. rubi*) were prepared by immersing the samples in epoxy resin at room temperature (23 °C). Then, the samples were stored for polymerization in a drying oven at 60 °C for 48 h. Slices of the scale cross-sections were cut using an ultramicrotome (Leica EM UC7). Then, the specimens were transferred onto copper grids for observation.

### CIE coordinate diagram

In this paper, CIE (Commission Internationale de l'Éclairage) 1931 normalized illuminant D65 was used as the standard. The CIE XYZ tristimulus values were calculated according to the simulated reflection  $R(\lambda)$  data. Then, the XYZ components were transformed into RGB components for imaging preparation. The last step was performing the color representation using MATLAB R2016a and replacing the RGB data with color points in the color map.

### Finite-difference time-domain simulations

The optical simulations were conducted with Lumerical FDTD Solutions software. The structural models were built using MATLAB R2016a and the FDTD program according to the numerical models mentioned below. The complex refractive index of chitin was set as  $1.56n + 0.06i$ , the reported value for butterfly scales. Here, we defined that numerical model  $f(x, y, z)$  out of the range of  $t$  denotes filling with air, and  $f(x, y, z)$  in the range of  $t$  denotes filling with chitin. The convergence test was performed, and the mesh size was chosen to obtain a good compromise between the required computer memory and the simulation time. A plane wave light source was used, and the incident angle was along the normal incidence direction. The periodic boundary condition was set in the  $x$  and  $y$  directions, while the perfectly matched layer was set in the  $z$  direction. The polarization direction was parallel to the  $x$ -axis.

### Thermodynamic measurements

The butterfly wings were placed on a metallic support in a vacuum chamber with a piece of foam to minimize thermal conduction and were fixed with specimen needles (Supplementary Fig. S1a). When exploring the change in wing temperature without the scales covered, the scales were removed carefully with an alcohol-soaked cotton swab. After wiping, there were no scales inserted into the membrane of the wing's ventral side (Supplementary Fig. S1c, d). A xenon lamp (X350) with an electronic switch was used to imitate the sunbeam. The increase and decrease of the wing temperature were recorded with an infrared thermal imaging camera (FLIR-T630c). A ZnSe window with high

transmittance in the middle infrared band was used to ensure the accuracy of the temperature records. The whole experimental setup is shown in Supplementary Fig. S1b.

## Results and discussion

### Morphology of *M. theseus* and numerical connotation

The wings of *M. theseus* are similar in size to those of other normal *Morpho* butterflies (Fig. 1a)<sup>31,32</sup>. The ventral side is covered with dense shiny silver scales occupying most of the area of the wing without any pigments (Fig. 1a). There are different colors ranging from red to blue on a single scale (Supplementary Fig. S2a, the scale in air), which are displayed as bright white due to the color mixing effect. The disordered tubular structures stack in different orientations from the top view of the scale (Fig. 1b), while cross-section images highlight the tubes in different helix degrees and their twining forms (Fig. 1c). Window-like architectures cover the surfaces of the scales, which provide mechanical support for the tube components below. These structural characteristics are partly consistent with the gyroid structure that is found in *C. rubi* blue-green scales (Fig. 1d). They are all distributed in tubular states with certain degrees of twining. In contrast, the gyroid architectures in *C. rubi* have a higher level of periodicity, regularity, and interconnected helices. The morphology of the *M. theseus* scales seems to be stuck in the process of gyroid spiraling. Reflection spectra results indicate that there is a relatively narrow reflection peak at 518 nm with an intensity of 29.83% for gyroid architectures, while the quasiordered, gyroid-like microstructures in *M. theseus* have wide-band reflection with high intensity. The average reflection in the visible light spectrum reaches 78.1%, which is fourfold higher than that of the gyroid domains (Fig. 1e). The reflectance variance of *M. theseus* is 2.75, while that of *C. rubi* is 9.42. Incredibly, the disordered tubular domains have a lower volume fraction (VF) of 10.24% on average, consisting only of chitin. To further prove that the whiteness is a result of architectures rather than pigments, a single scale of *Morpho theseus* was immersed in bromoform, of which the refractive index is close to chitin ( $n \approx 1.56$ ). After immersion, the scale became semitransparent, and color pixels disappeared (Supplementary Fig. S2a). With bromoform evaporation, the average reflectivity increased from less than 10 to 78%, which was the value before immersion (Supplementary Fig. S2b). To investigate the observation angle dependence of *M. theseus*, a microangle-resolved reflectance spectra test was implemented. The results show that under all observation angles, there is no significant drop in the visible band. The average reflection can still be maintained at 63.75% at an observation angle of  $\pm 60^\circ$ , which demonstrates the low viewing angle dependence (Fig. 1f).

As mentioned above, there is a correlation between the *M. theseus* wing scale architecture and *C. rubi* wing scale gyroid texture in terms of morphology. They are all

distributed in tubular states but are different in terms of regularity and twining forms. Through numerical analysis, it is seen that there is still a common peculiarity between the tubes and gyroid in terms of mathematics (Fig. 2). After the discovery of the gyroid minimal surface in lipid–water systems<sup>33</sup> in 1967, the mathematical model was soon precisely defined by Schoen as<sup>34</sup>

$$\sin(x) \cos(y) + \sin(y) \cos(z) + \sin(z) \cos(x) = t (|t| \leq 1.5) \quad (1)$$

where  $x$ ,  $y$ , and  $z$  are equal to  $2\pi X/T$ ,  $2\pi Y/T$ , and  $2\pi Z/T$ , respectively;  $(X, Y, Z)$  are the coordinates of a specific point in the cubic unit cell,  $t$  is related to the VF, and  $T$  determines the unit cell size.

In Eq. (1), the subtrigonometric element  $\sin(x) \cos(y)$  exactly expresses the tubular structure as

$$f_{\text{tub}}(x, y, z) = \sin(\omega_1 x) \cos(\omega_1 y) = t_{\text{tub}} (t_{\text{tub}} \geq a_{\text{tub}}) \quad (2)$$

where  $\omega_1$  represents  $2\pi/T_{\text{tub}}$ . Expressions of  $S_{\text{tub}}$  (size of the tube) and  $D_{\text{tub}}$  (the distance between centers of nearest tubes) are given by (details given in Supplementary text and Supplementary Fig. S3)

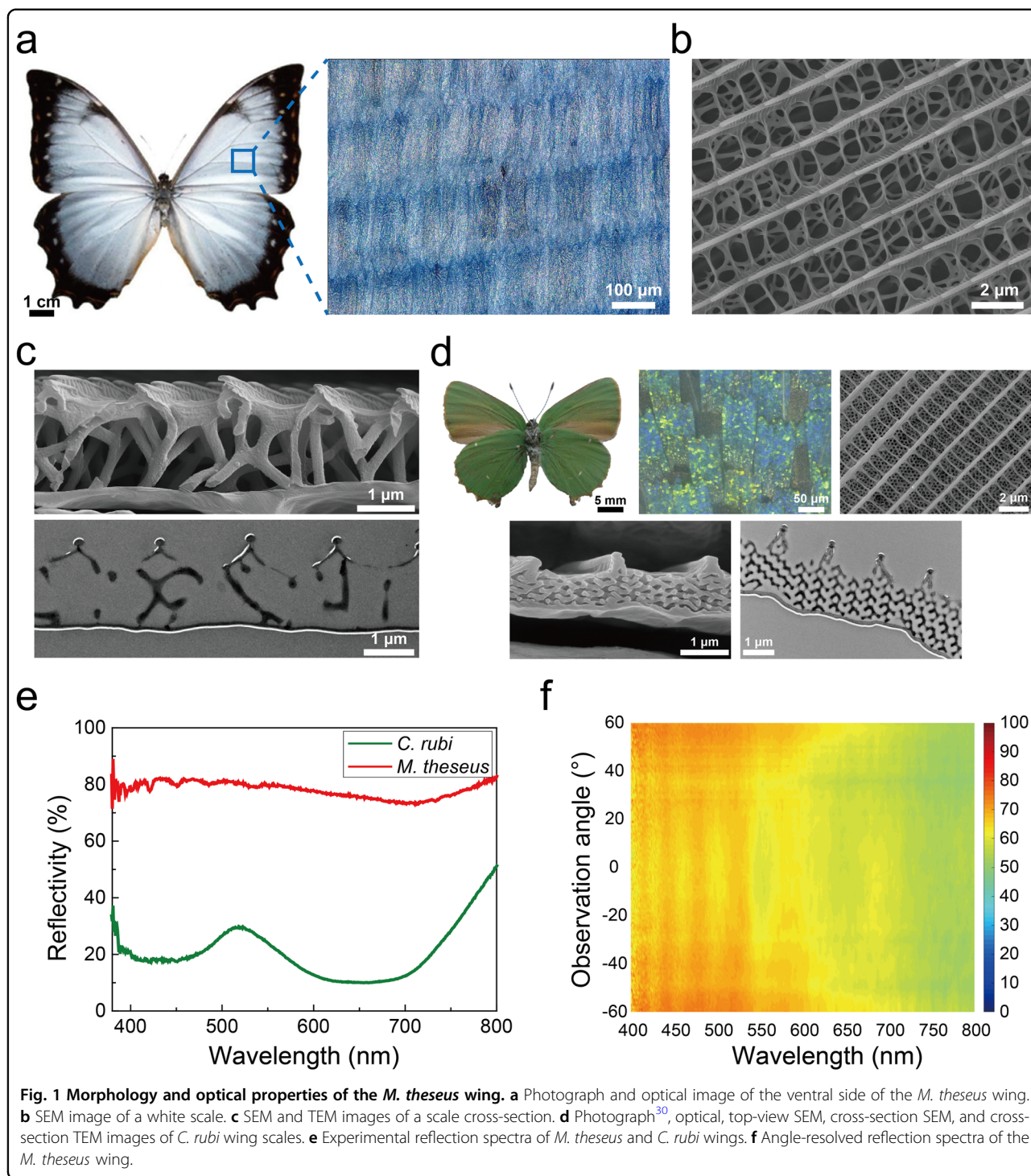
$$S_{\text{tub}} = \left( \frac{1}{2} - \frac{1}{\pi} \sin^{-1} a_{\text{tub}} \right) \cdot T_{\text{tub}} \quad (3)$$

$$D_{\text{tub}} = \frac{\sqrt{2} T_{\text{tub}}}{2} \quad (4)$$

From a mathematical perspective, the correlation between tubular and gyroid structures has been further proven (Fig. 2). In *M. theseus*, the tubular architectures are distributed in terms of diversity but are in a quasiordered arrangement (Fig. 1b and c). Next, we will discuss the numerical model of the *M. theseus* structure and its optical performance.

### Numerical model and optical simulation of *M. theseus* architectures

According to structural and numerical analysis, *M. theseus* scale architectures have various tubular characteristics with different helix degrees, twining forms, and orientations. In addition, the period and VF are also in disordered distributions. The multiple morphologies of the tubular forms, periods, and VFs lead to diversity in the reflection bands and intensities. From the macroscopic view, the scales appear bright white. For tubular form difference characterization, coefficients  $A$ ,  $B$ , and  $C$  are

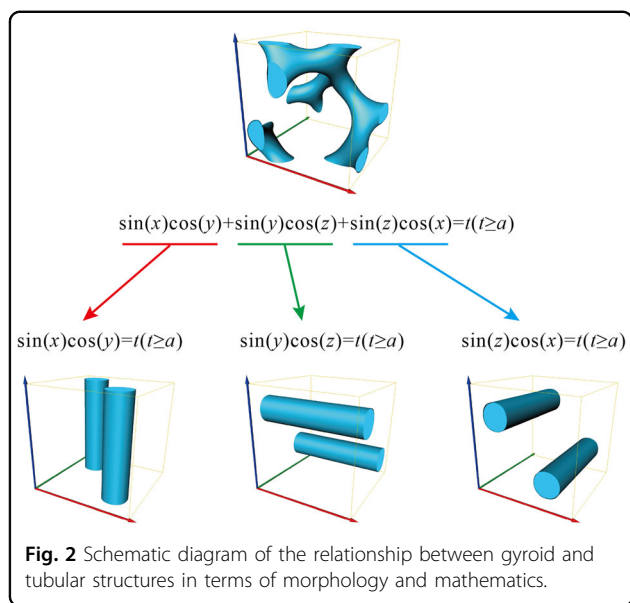


introduced in the gyroid model as

$$A \cdot \sin(x) \cos(y) + B \cdot \sin(y) \cos(z) + C \cdot \sin(z) \cos(x) = t (t \geq a) \tag{5}$$

Mathematically, the percentage of *A*, *B*, and *C* determines the twining and helix forms of the tubes. In the following, we

use the (*A*, *B*, *C*) format to denote the values of the three coefficients. It is clear that (1, 0, 0) matches simple tubes, while (1, 1, 1) matches the 3D gyroid structure. In *M. theseus* wing scales, there are various tubular states between (1, 0, 0) and (1, 1, 1). Furthermore, we summarize the representative coefficient arrays in the numerical phase diagram (Fig. 3b). Since we are concerned with the proportion of the three



subtrigonometric elements that affect the tubular form, all arrays are normalized for convenience. The corresponding structural models are shown in Fig. 3a. Statistical results show that the period (cubic unit cell size) of *M. theuseus* microstructures differs in the range of 326–1063 nm (Supplementary Fig. S4 and Supplementary Table S1), with the VF ranging from 5.00 to 16.22% (Supplementary Fig. S5 and Supplementary Table S2). The structures in Fig. 3a maintain the same period of 600 nm and a VF of 11%.

Structures with the same coefficient proportions, such as (1, 0, 0), (0, 1, 0), and (0, 0, 1), have the same configuration characteristics but different orientations. Starting from straight tubes, they gradually twist with the other two coefficients increasing. When the coefficients are (1, 1, 0), two of the three structural elements have the same proportion. At this moment, adjacent curved tubes interconnect and evolve into 3D architectures with a helical prototype. Finally, the gyroid structure is generated with a high level of interconnected helices, and the three numerical elements in Eq. (5) have the same proportion.

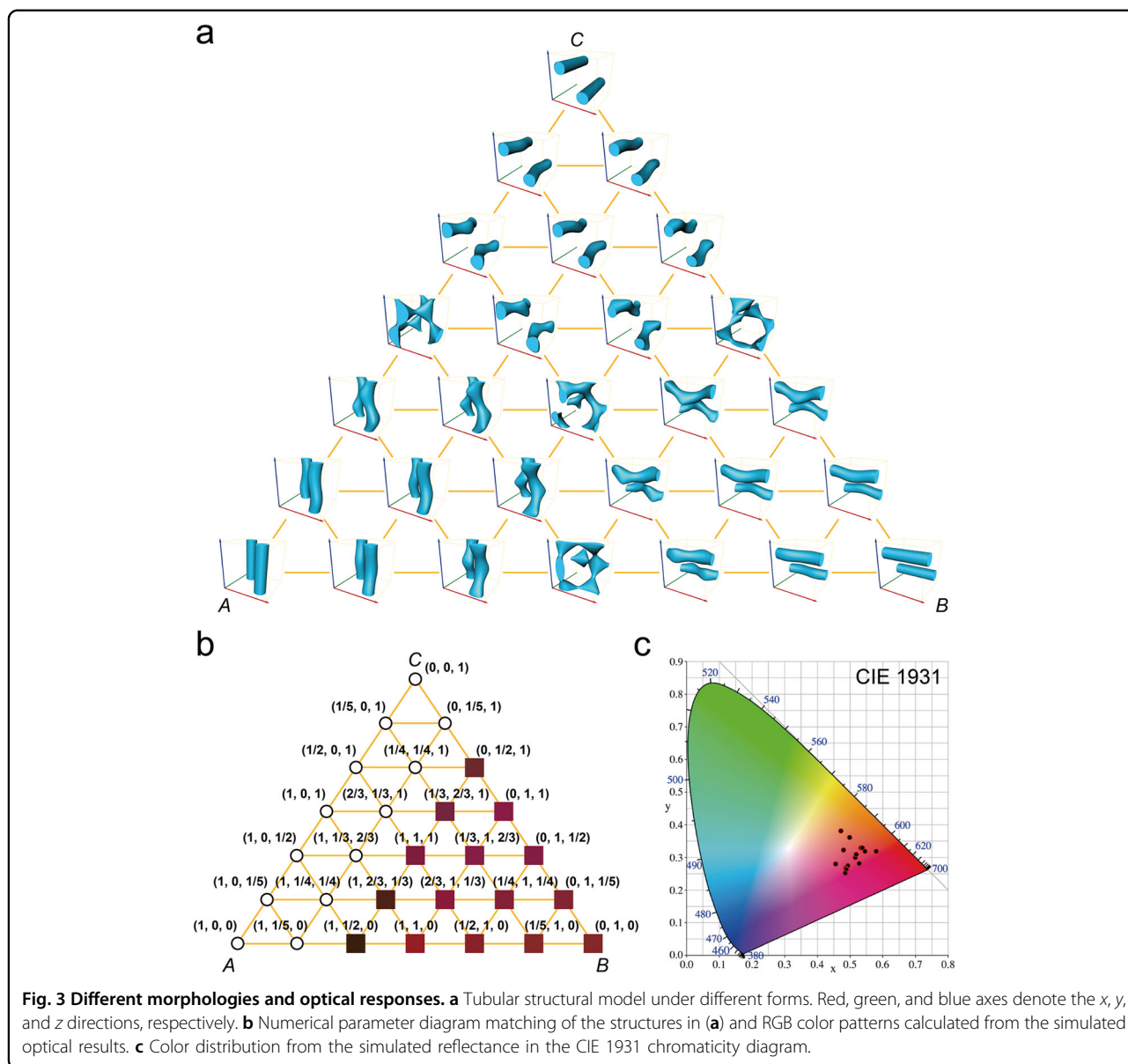
The results of the optical simulation under normal incidence show that the anisotropy of the tubular structure results in a reflection difference (Supplementary Fig. S6a–g). When the tubular orientation is perpendicular to the polarization direction, the structures have high transmission in the visible band with an average reflectivity of less than 5% (Supplementary Fig. S6a–g). As the tubes are oriented parallel to the polarization direction, reflection peaks appear in the wavelengths between 623 and 670 nm, which is the red range (Supplementary Fig. S6a–g). Color patterns are present on the relevant phase diagram position according to the RGB value calculation (Fig. 3b). In the diagram, the filling color of the box at the nodes is the corresponding calculation color. “O” denotes the structures with high transmission in the

visible band without obvious color. Notably, the peaks gradually narrow with the optimization of the tubular structure spiraling, demonstrating increased color saturation (Supplementary Fig. S6h). Then, the peak values are transformed into the CIE (Commission Internationale de l’Eclairage) 1931 chromaticity diagram (Fig. 3c). Most of the color coordinates are in the red region and close to the edge of the chromaticity diagram. Overall, there is a high level of vividness for ordered structures with different tubular forms, which leads to high brightness when viewed on a macroscopic scale. Structures with a higher degree of helicity have better color saturation.

When the period is defined at 600 nm, the color distribution of different structural morphologies is mainly concentrated in the same color range. As the unit cell size changes, the color response is more sensitive. Here, the tubular orientation is controlled to be parallel to the polarization direction, and VF remains constant at 11%. The results of the simulated reflection show that there is a uniform redshift of the peak position as the unit cell size increases (Fig. 4a–c). The regularity is universal in the other morphologies (Supplementary Fig. S7). As the periods of the structures change from 300 to 1000 nm, the peak width at state (0, 1, 0) exhibits linear expansion from 56 to 195 nm, while the peak position moves from 311 to 1038 nm (Fig. 4a). The gradient trend slows with a higher degree of structural helicity (Fig. 4d). During the process, the peak value remains almost constant at 64%, 58%, and 36% for states (0, 1, 0), (1, 1, 0), and (1, 1, 1), respectively (Fig. 4d). As shown in the CIE chromaticity diagram (Fig. 4e), the diversity in the periods allows the architectures of *M. theuseus* scales to include seven broad categories of colors in the visible range. In addition, structures with smaller unit cell sizes produce higher saturation colors.

The VF of the structure is another important factor affecting the optical performance. For most morphologies in Fig. 3a, the VF tuning determines the diameter of the tubular structures. In particular, there is a peculiar morphology at (2/3, 1, 1/3). In addition to the tubular features, the structure has a certain degree of curvature, which causes not only the expansion of the diameter but also the interconnection of adjacent curved tubes as the VF rises (Fig. 4f). The reflection results indicate that as the structural VF increases from the initial value of 5%, the peak reflectance rises from 46.44% with the position moving to the red band region. When VF reaches 16%, the peak reflectance increases to 59.4% at 668 nm (Fig. 4g), accompanied by the broadening of the peak width. Moreover, the reflection peak with a lower intensity at approximately 400 nm gradually disappears with increasing VF.

In summary, the tubular form, period, and VF of the architectures simultaneously lead to color diversity. For tubular forms, the color response exhibits anisotropic characteristics. Structures with a tubular orientation perpendicular to the polarization direction have high transmittance.



For the structures with tubular orientation along the polarization direction, the reflection peaks mostly appear in the same color region. Better color saturation corresponds to tubes with a higher degree of helicity. The color response of the structure is particularly sensitive to its period. As the period increases, the reflection peak is redshifted, and the amplitude is approximately consistent with that of the period. The VF affects both the reflection intensity and peak position. As the VF increases, the reflection intensity of the structure increases with the peak position moving toward the long wavelength band. It appears as bright structural whiteness in *M. theseus* wing scales from the macroscopic view due to the multiple morphologies.

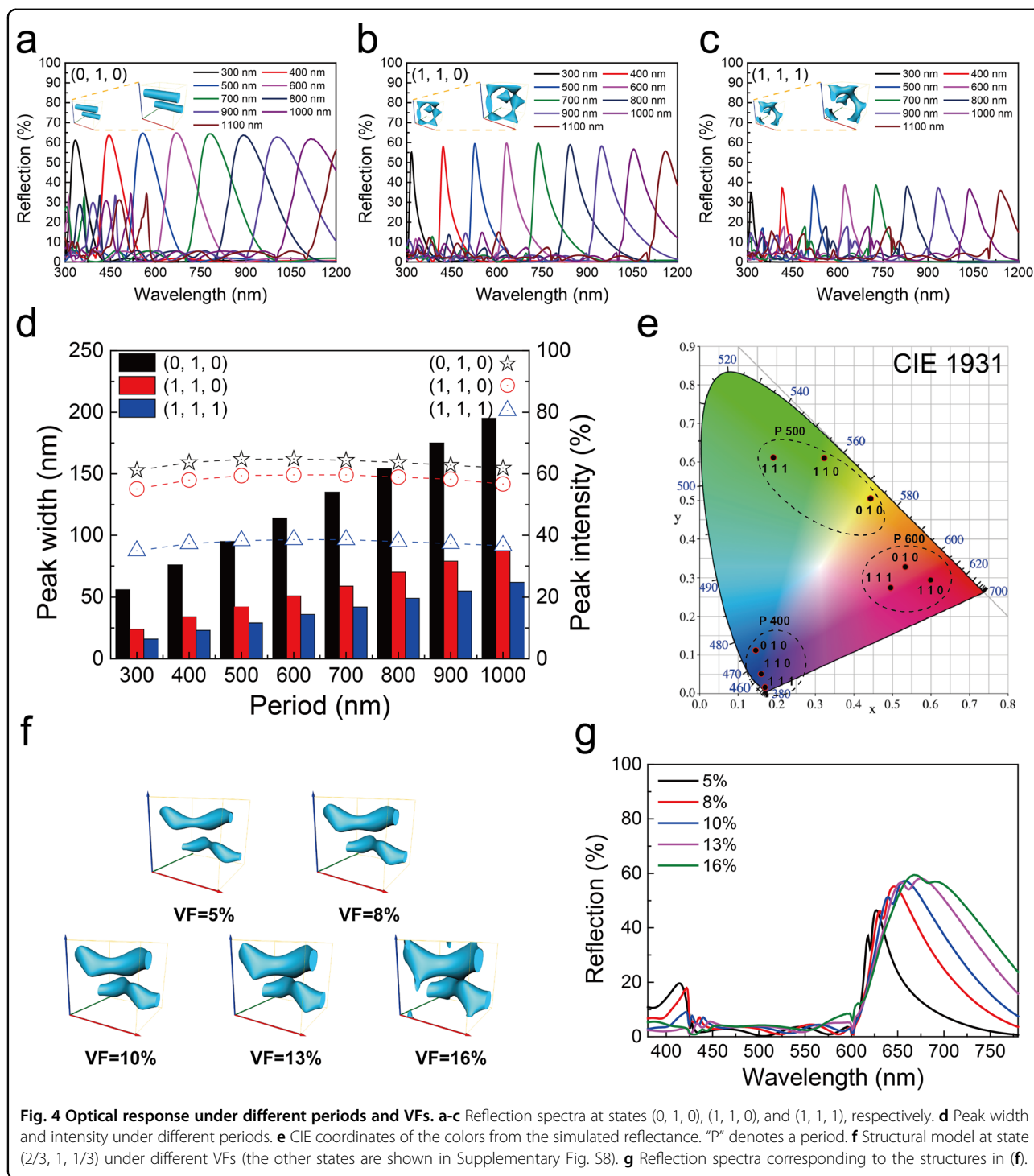
To further modify the numerical model for a more precise description of the structures' quasicrystalline

characteristics, disordered factors are introduced in Eq. (5) as

$$A_{nrand} \cdot \sin(x) \cos(y) + B_{nrand} \cdot \sin(y) \cos(z) + C_{nrand} \cdot \sin(z) \cos(x) = t (t \geq a_{nrand}) \tag{6}$$

$$\begin{cases} A_{nrand} = \frac{A_{rand}}{\max(A_{rand}, B_{rand}, C_{rand})} \\ B_{nrand} = \frac{B_{rand}}{\max(A_{rand}, B_{rand}, C_{rand})} \\ C_{nrand} = \frac{C_{rand}}{\max(A_{rand}, B_{rand}, C_{rand})} \end{cases} \begin{cases} A_{rand} = rand(0, 1) \\ B_{rand} = rand(0, 1) \\ C_{rand} = rand(0, 1) \end{cases} \tag{7}$$

where  $rand(0, 1)$  denotes a randomly generated number between 0 and 1,  $\max(A_{rand}, B_{rand}, C_{rand})$  represents the maximum values of  $A_{rand}$ ,  $B_{rand}$ , and  $C_{rand}$ , and  $x$ ,  $y$ , and  $z$

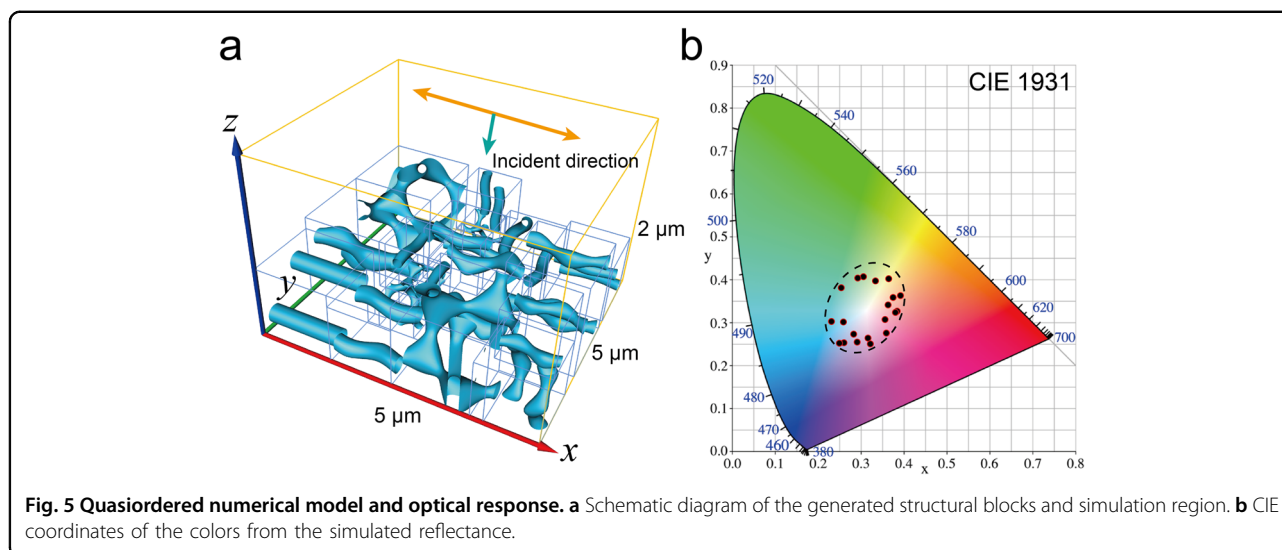


are equal to  $2\pi X/T_{rand}$ ,  $2\pi Y/T_{rand}$ , and  $2\pi Z/T_{rand}$  respectively.  $T_{rand}$  is a randomly generated number between 326 and 1063 nm (period distribution), defined as

$$T_{rand} = rand(326, 1063) \tag{8}$$

where  $a_{rand}$  corresponds to a randomly generated VF value between 5.00 and 16.22%.

As shown in the schematic diagram (Fig. 5a and Supplementary Movie S1), the single-period structural blocks generated based on Eq. (6) are imported into the simulation region in a densely stacked form. The size of the simulation region is  $5 \times 5 \times 2 \mu\text{m}$  in the  $x$ ,  $y$ , and  $z$  directions, respectively, which achieves a good compromise in terms of computing power. Notably, the larger the



simulation area in the  $x$  and  $y$  directions, the closer the module is to the quasiordered morphology of the scales. We performed independent simulations 20 times to avoid the accidental error caused by small samples. Then, the simulated reflectance data were converted to the CIE chromaticity diagram (Fig. 5b). Most color coordinates are close to the central white point, which demonstrates the color mixing effect due to quasiordered tubular structures.

In future work, for much better matching with the architectures of the *M. theseus* scales, the numerical model can be further improved as follows: (1) the orientation of the tubes can be discussed omnidirectionally rather than just along the  $x$ ,  $y$ , and  $z$  directions. The rotation elements can be introduced into the numerical model imitated in the Supplementary text and Supplementary Fig. S9. (2) The period and VF distributions are regarded as equal probability in this work, and the real distribution in scales can be counted and coupled into our numerical model. In addition, some structural factors with little influence on the optical performance can be ignored, such as surface roughness and the scale's lower lamina thickness. Considering that the surface roughness size of tubular structures is much smaller than the visible wavelength, we simplified the surface of all tubular structures to the smooth state in the modeling process. For the scale's lower lamina thickness, the simulated spectral results show that the optical performances have little change, regardless of whether the lower lamina thickness is considered (Supplementary Fig. S10).

In summary, the numerical model presented herein provides a feasible route for depicting the quasiordered architectures of butterfly scales through the combination of a periodic numerical framework and random elements. In nature, most microstructural arrays in organisms are

accompanied by slightly disordered doping. Previous works have demonstrated the advantages of quasiordered characteristics<sup>35–37</sup>. The methodology involved in our model is beneficial for facilitating more in-depth studies of the performance improvement brought about by other quasiordered structures. Moreover, compared with other strategies for achieving structural white, the advantages of the quasiordered structures in this paper are as follows: (1) The structural parameters can be controlled within a certain range. The robustness of the quasiordered structure is resilient against small fabrication imperfections, which is conducive to mass fabrication. (2) The structure has a lower observation angle dependence. (3) The broadband reflection of sunlight can be achieved with a low volume fraction (16% on average), which is efficient in terms of saving materials.

#### The cooling effect of *M. theseus* wings

Structural white can efficiently regulate body temperature when butterflies are exposed to a direct sunlight environment. To investigate the cooling effect of the scales covering the wings, thermodynamic experiments were conducted to mimic the temperature changes in butterfly wings exposed to sunlight. A high-power xenon lamp was used to imitate sunbeams, and the temperature changes were recorded with an infrared thermal imaging camera. The white area of the hindwing was clipped and placed on the metallic support in the vacuum chamber with a piece of foam to reduce thermal conduction. The results of the thermodynamic experiments comparing the states of the wing covered with scales and the wing with scales removed reveal that the white scales can significantly reduce the surface temperature of the wings (Fig. 6a, b). Compared with the wing without scales, the wing covered with scales in air has an equilibrium



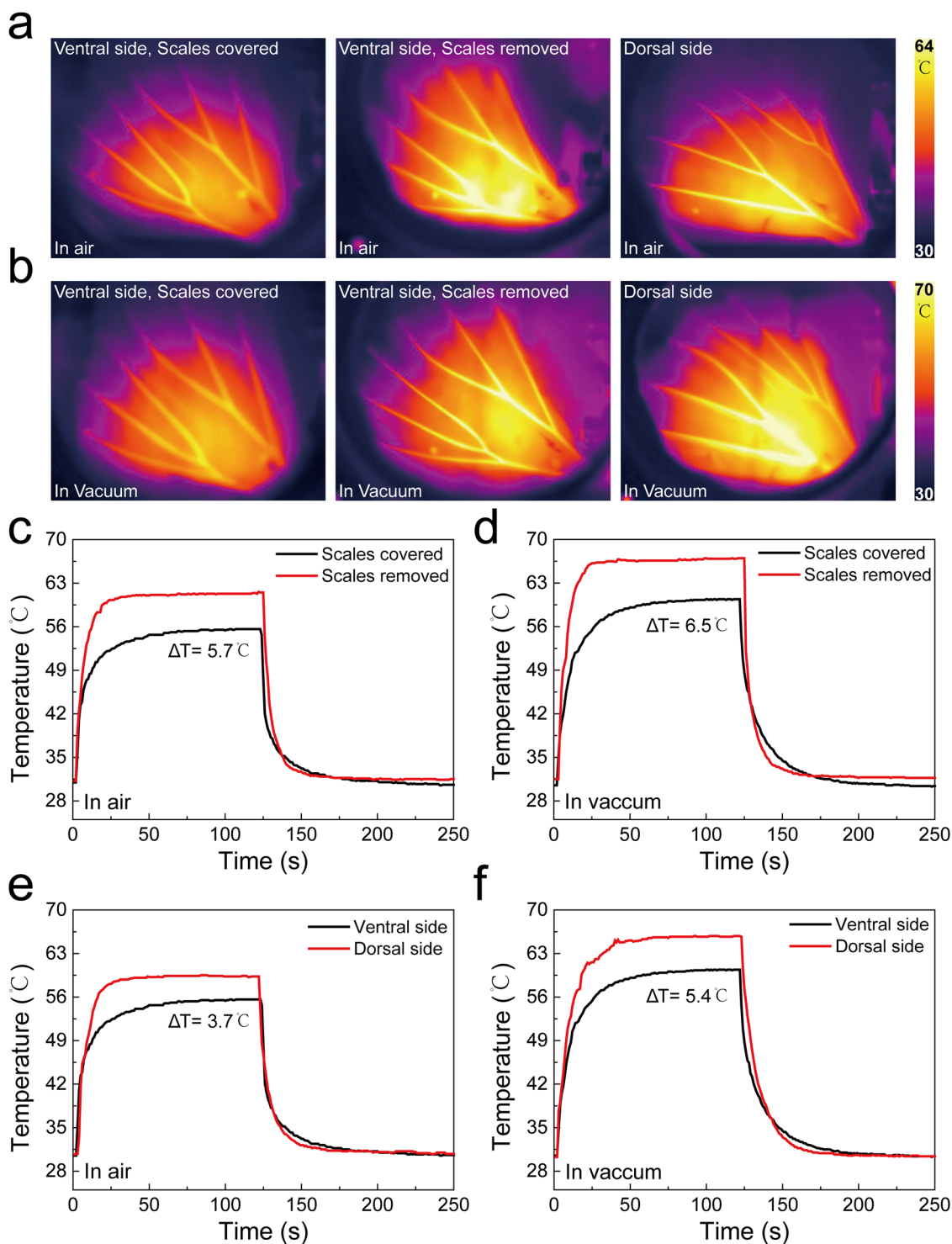


**Fig. 6 Thermodynamic experimental results.** **a** Thermal camera images of the scales of the ventral side of the wing covered and removed and of the dorsal side in still air. **b** Thermal camera images of the scales of the ventral side of the wing covered and removed and of the dorsal side under vacuum. **c, d** Temporal temperature profiles of the wing covered with scales and with scales removed under air and vacuum conditions, respectively. **e, f** Temporal temperature profiles of the ventral and dorsal sides of the wing under air and vacuum conditions, respectively.

temperature that can be reduced by 5.7 °C (Fig. 6c). The cooling effect is more significant under vacuum conditions, with an equilibrium temperature drop of 6.5 °C due to the eliminated convective heat transfer (Fig. 6d). In addition, we also compared the thermal response between the white ventral side and dark brown dorsal side of the *M. theseus* wing. The difference in equilibrium temperature is 3.7 °C in air (Fig. 6e) and 5.4 °C (Fig. 6f) under vacuum. The wing color characteristic of white and dark on different sides is a crucial tool for flexible thermal management under different conditions. To prevent risks of overheating and cell damage from direct solar radiation, wings with white scales can be spread for enhanced reflectivity in the visible light spectrum. Undoubtedly, using structural white for cooling is energy efficient.

## Conclusion

To summarize, the visible broadband reflection of *M. theseus* wings is induced by quasioordered tubular architectures in the scales, which are distributed in different orientations and twining forms. Furthermore, we revealed the correlation between straight tubes and the gyroid structure from a mathematical perspective. Through numerical analysis, it was found that *M. theseus* scale architectures have different tubular distributions between straight tubes and gyroid structures. The simulated results indicated that the diversity of the tubular form, period, and VF of the architecture in the scales led to color diversity. From the macroscopic view, the butterfly wings display bright structural whiteness. Subsequently, using the numerical model built with the combination of a periodic numerical framework and random elements, we confirmed that the structural whiteness resulted from the color mixing effect. In addition, the quasioordered characteristic of the architectures was well expressed. Thermodynamic experiments indicated that white scales can efficiently help reduce the temperature of butterfly wings to prevent the risks of overheating from direct sunlight. Inspired by the structural whiteness in *M. theseus*, there is great application potential for the design of efficient and energy-saving materials with certain structures. Our work provides new insight into the mathematical description of quasioordered structures by concise rules. The methodology developed by this numerical model can facilitate a deep understanding of the performance improvement brought by quasioordered structural characteristics. Corresponding solutions can guide the design of advanced photonic devices to achieve cooling, camouflage, and photothermal conversion.

## Acknowledgements

We are grateful to X.H. Liu for the careful comments that improved this manuscript. This research was supported by the Top Young Talents of Ten Thousand Talents Plan, National Natural Science Foundation of China

(51971133, 51801121, 51902200, and 52072241), and the Shanghai Science and Technology Committee (19JC1410400, 19ZR1425100).

## Author contributions

W.Z. and D.Z. conceived the idea of this study. X.Z. designed and executed the experiments and analyzed the data. Y.X. helped build the mathematical models and conduct the experiments. X.Z. and W.W. designed the optical modeling and analyzed the results. X.Z. wrote the manuscript, and all the authors revised the manuscript. W.Z. and W.W. directed the research.

## Competing interests

The authors declare no competing interests.

## Publisher's note

Springer Nature remains neutral with regard to jurisdictional claims in published maps and institutional affiliations.

**Supplementary information** The online version contains supplementary material available at <https://doi.org/10.1038/s41427-023-00463-2>.

Received: 31 July 2022 Revised: 18 December 2022 Accepted: 4 January 2023.

Published online: 31 March 2023

## References

- Cao, X. et al. Replicating the *Cynandra opis* butterfly's structural color for bioinspired bigrating color filters. *Adv. Mater.* **34**, e2109161 (2022).
- Hu, Y., Wei, B., Yang, D., Ma, D. & Huang, S. Chameleon-inspired brilliant and sensitive mechano-chromic photonic skins for self-reporting the strains of earthworms. *ACS Appl. Mater. Interfaces* **14**, 11672–11680 (2022).
- Miao, W., Tian, Y. & Jiang, L. Bioinspired superspreading surface: from essential mechanism to application. *Accounts Chem. Res.* **55**, 1467–1479 (2022).
- Ying, P. et al. A bio-inspired nanocomposite membrane with improved light-trapping and salt-rejecting performance for solar-driven interfacial evaporation applications. *Nano Energy* **89**, 106443 (2021).
- Shi, N. N. et al. Keeping cool: enhanced optical reflection and radiative heat dissipation in Saharan silver ants. *Science* **349**, 298–301 (2015).
- Vukusic, P., Hallam, B. & Noyes, J. Brilliant whiteness in ultrathin beetle scales. *Science* **315**, 348 (2007).
- Wang, S. et al. Biologically inspired scalable-manufactured dual-layer coating with a hierarchical micropattern for highly efficient passive radiative cooling and robust superhydrophobicity. *ACS Appl. Mater. Interfaces* **13**, 21888–21897 (2021).
- Yang, Z. & Zhang, J. Bioinspired radiative cooling structure with randomly stacked fibers for efficient all-day passive cooling. *ACS Appl. Mater. Interfaces* **13**, 43387–43395 (2021).
- Syurik, J. et al. Bio-inspired, large scale, highly-scattering films for nanoparticle-alternative white surfaces. *Sci. Rep.* **7**, 46637 (2017).
- Mandal, J. et al. Hierarchically porous polymer coatings for highly efficient passive daytime radiative cooling. *Science* **362**, 315–318 (2018).
- Xiang, B. et al. 3D porous polymer film with designed pore architecture and auto-deposited SiO<sub>2</sub> for highly efficient passive radiative cooling. *Nano Energy* **81**, 105600 (2021).
- Mäthger, L. M. et al. Bright white scattering from protein spheres in color changing, flexible cuttlefish skin. *Adv. Funct. Mater.* **23**, 3980–3989 (2013).
- Zhai, Y. et al. Scalable-manufactured randomized glass-polymer hybrid metamaterial for daytime radiative cooling. *Science* **355**, 1062–1066 (2017).
- Syurik, J., Jacucci, G., Onelli, O. D., Hölscher, H. & Vignolini, S. Bio-inspired highly scattering networks via polymer phase separation. *Adv. Funct. Mater.* **28**, 1706901 (2018).
- Wilts, B. D. et al. Evolutionary-optimized photonic network structure in white beetle wing scales. *Adv. Mater.* **30**, e1702057 (2018).
- Cai, L. et al. Spectrally selective nanocomposite textile for outdoor personal cooling. *Adv. Mater.* **30**, e1802152 (2018).
- Zhou, K. et al. Three-dimensional printable nanoporous polymer matrix composites for daytime radiative cooling. *Nano Lett* **21**, 1493–1499 (2021).

18. Liu, X. et al. Bright silver brilliancy from irregular microstructures in butterfly *Curetis acuta* Moore. *Adv. Opt. Mater.* **7**, 1900687 (2019).
19. Vukusic, P., Kelly, R. & Hooper, I. A biological sub-micron thickness optical broadband reflector characterized using both light and microwaves. *J. R. Soc. Interface* **6**, S193–S201 (2009).
20. Zhang, H. et al. Biologically inspired flexible photonic films for efficient passive radiative cooling. *Proc. Natl Acad. Sci. USA* **117**, 14657–14666 (2020).
21. Rephaeli, E., Raman, A. & Fan, S. Ultrabroadband photonic structures to achieve high-performance daytime radiative cooling. *Nano Lett* **13**, 1457–1461 (2013).
22. Wang, W. L. et al. Self-adaptive radiative cooling and solar heating based on a compound metasurface. *J. Mater. Chem. C* **8**, 3192–3199 (2020).
23. Zhao, B., Hu, M., Ao, X., Xuan, Q. & Pei, G. Comprehensive photonic approach for diurnal photovoltaic and nocturnal radiative cooling. *Sol. Energy Mater. Sol. Cells* **178**, 266–272 (2018).
24. Zhao, X. et al. Optical optimization with microstructure evolution inspired from lepidopteran scales. *Adv. Opt. Mater.* **10**, 2200710 (2022).
25. Davis, A. L., Nijhout, H. F. & Johnsen, S. Diverse nanostructures underlie thin ultra-black scales in butterflies. *Nat. Commun.* **11**, 1294 (2020).
26. Krishna, A. et al. Infrared optical and thermal properties of microstructures in butterfly wings. *Proc. Natl Acad. Sci. USA* **117**, 1566–1572 (2020).
27. Tsai, C. C. et al. Physical and behavioral adaptations to prevent overheating of the living wings of butterflies. *Nat. Commun.* **11**, 551 (2020).
28. Wilts, B. D., Matsushita, A., Arikawa, K. & Stavenga, D. G. Spectrally tuned structural and pigmentary coloration of birdwing butterfly wing scales. *J. R. Soc. Interface* **12**, 20150717 (2015).
29. Kjellstrom, T. & Crowe, J. Climate change, workplace heat exposure, and occupational health and productivity in Central America. *Int. J. Occup. Environ. Health* **17**, 270–281 (2011).
30. Wu, L. et al. Highly sensitive, reproducible and uniform SERS substrates with a high density of three-dimensionally distributed hotspots: gyroid-structured Au periodic metallic materials. *NPG Asia Mater.* **10**, e462 (2018).
31. Fang, J. et al. Three-dimensional CdS/Au butterfly wing scales with hierarchical rib structures for plasmon-enhanced photocatalytic hydrogen production. *ACS Appl. Mater. Interfaces* **10**, 19649–19655 (2018).
32. Lal, N. N. et al. Transparent long-pass filter with short-wavelength scattering based on *Morpho* butterfly nanostructures. *ACS Photonics* **4**, 741–745 (2017).
33. Luzzati, V. & Spegel, P. A. Polymorphism of lipids. *Nature* **215**, 701–704 (1967).
34. Schoen, A. H. *Infinite Periodic Minimal Surfaces Without Self-intersections*. Report No. NASA-TN-D-5541 (National Aeronautics and Space Administration, 1970).
35. Rothhammer, M., Zollfrank, C., Busch, K. & von Freymann, G. Tailored disorder in photonics: learning from nature. *Adv. Opt. Mater.* **9**, 2100787 (2021).
36. Wang, W. et al. Omnidirectional light absorption of disordered nano-hole structure inspired from *Papilio ulysses*. *Opt. Lett.* **39**, 4208 (2014).
37. Wang, W. et al. Design of a structure with low incident and viewing angle dependence inspired by *Morpho* butterflies. *Sci. Rep.* **3**, 3427 (2013).